Energy Technology
Generation, Conversion, Storage, Distribution
www.entechnol.de

Rational Choice of Amide-Based Electrolytes Toward High-Power Rechargeable Lithium-Air Batteries

Akihiro Nomura, Shota Azuma, Fumisato Ozawa, and Morihiro Saito*

Lithium–air batteries (LABs) are a promising technology for high-energy-density battery storage. However, their open-cell structure for oxygen exchange leads to electrolyte evaporation, which limits cycling performance under ambient conditions. Herein, volatile amide-based electrolytes for LABs using gravimetric analysis are evaluated. The cell weight change during discharge–charge cycles confirms the two-electron oxygen reduction/evolution reactions while also revealing that electrolyte evaporation correlates with the solvent vapor pressure. This behavior significantly compromises the cycle performance of low-viscosity amide electrolyte cells. Despite this, rate-dependent cycling experiments demonstrate the superior cyclability of the low-viscosity amide electrolyte cells at high current rates (0.8 mA cm^{-2} or higher), conditions under which cells with a conventional tetraethylene glycol dimethyl ether (TEG)-based LAB electrolyte fail. Scanning electron microscopy and X-ray diffraction analyses show that these cells exhibit improved rechargeability at high-rate cycles, with discharge product morphology changing to a more easily decomposable form. This electrolyte design strategy marks a significant advancement toward developing high-power, high-energy rechargeable LABs.

1. Introduction

The growing demand for high-energy-density energy storage has driven research into lithium–air batteries (LABs), which generate electricity through the aerobic oxidation of lithium, offering a high theoretical energy density of 3,500 Wh kg^{-1} (including oxygen mass).[1] Recent advancements in LAB materials and cell assembly have led to the development of LAB cells with Ah-class capacities and energy densities ranging from 500 to 1000 Wh kg^{-1}.[2–5] Despite these achievements, high-energy-density LABs are hindered by extremely low power output. Although their capacity per unit weight is high, limited discharge current rates, typically less than 0.5 mA cm^{-2} per unit electrode area, result in a power density of 100 W kg^{-1} or less, which remains lower than that of lead-acid batteries. Besides, the sluggish oxygen reduction reaction (ORR) requires a high oxygen partial pressure during discharge. Under normal air conditions with a ≈21% oxygen gas concentration, discharge performance deteriorates.[6] These factors severely limit the commercialization of LABs, making the enhancement of their power output an urgent challenge.

Because battery power is directly linked to the discharge current rate, researchers have strived to enhance discharge current capabilities by supporting ORR catalysts on the cathode surface[7,8] or introducing ORR redox mediators into the electrolyte.[9] However, their practical applicability in practical LAB systems remains controversial, as they require substantial material loading to achieve catalytic effects, which increases cell weight and compromises the high-energy-density nature of LABs. Alternatively, some studies have improved the discharge performance through cathode design and electrolyte composition, including the open-cell system in air batteries that require oxygen gas exchange.[10–14] Cathode pore architecture significantly affects the discharge performance. A high surface area cathode provides an extensive ORR surface, enabling efficient current generation. The distribution of cathode pores ensures a smooth supply of Li^+ and oxygen to the ORR surface, facilitating battery reactions and enhancing cell capacities.[10–12] Electrolytes also contribute to improved rate capability by facilitating reactant supply. It has been reported that the oxygen solubility and diffusion in electrolytes positively influence discharge performance.[5,13,14] Given the typically low solubility of oxygen (a few ppm) in most liquid electrolyte solvents, the oxygen supply is more critical than Li^+ transfer in the LABs. By utilizing highly porous, high surface area cathodes combined with low-viscosity amide-based electrolytes that facilitate fast oxygen diffusion, we recently demonstrated a discharge current rate of 5.0 mAh cm^{-2} in LAB cells under dry air conditions.[15] This resulted in a

A. Nomura, S. Azuma
Research Center for Energy and Environmental Materials
National Institute for Materials Science
1-1 Namiki, Tsukuba, Ibaraki 305-0044, Japan
E-mail: NOMURA.Akihiro@nims.go.jp

S. Azuma, F. Ozawa, M. Saito
Department of Science and Technology
Faculty of Science and Technology
Seikei University
3-3-1 Kichijoji-Kitamachi, Musashino, Tokyo 180-8633, Japan

S. Azuma
National Institute of Technology
Tokyo College
1220-2 Kunugida-machi, Hachioji, Tokyo 193-0997, Japan

The ORCID identification number(s) for the author(s) of this article can be found under https://doi.org/10.1002/ente.202500556.

DOI: 10.1002/ente.202500556

discharge capacity of 3.5 mAh cm^{-2}, nearly twice the capacity of lithium-ion batteries (LiBs, ≈2 mAh cm^{-2}), encouraging the development of a "true" LAB capable of operating in ambient air.

For rechargeable LABs, achieving good cyclability relies on oxidative tolerance against active oxygen species and electrochemical inertness within the battery voltage range. Since the discovery of the reversible deposition and decomposition of lithium peroxide (Li_2O_2) on a carbon cathode with ether-based electrolytes,[16,17] tetraethylene glycol dimethyl ether (TEG)-containing lithium bis(trifluoromethanesulfonyl)imide (LiTFSI) has become a standard electrolyte in many LAB studies.[3–13] The high boiling point of TEG (275 °C) effectively suppresses electrolyte volatilization in the semi-open cell system, supporting long-term discharge–charge cycle operations under continuous gas flow. However, the high viscosity of TEG-based electrolytes limits their current rate capabilities.[15] In contrast, amide-based electrolytes, which also enable reversible Li_2O_2 deposition and decomposition,[18–22] have a lower viscosity compared to TEG-based electrolytes, presenting a potential breakthrough for high-power rechargeable LABs. Additionally, amides are expected to exhibit greater tolerance to active oxygen species than ethers,[23] which could enhance improved cyclability in LABs. However, the narrow voltage window and high volatility of amide-based electrolytes limit their use in open-cell LAB systems. Although lithium nitrate ($LiNO_3$) or lithium nitrite ($LiNO_2$) as supporting salts improves the compatibility of amides as electrolyte solvents by forming a high-quality solid electrolyte interphase (SEI) on the Li anode,[22] they do not address the volatility issue. Electrolyte evaporation is particularly problematic under lean electrolyte conditions, which is necessary for achieving high energy and power densities in LABs.[24] To avoid solvent volatilization, some studies have used closed-cell systems filled with pure oxygen,[25] but this approach does not align with the practical need for lightweight batteries that operate in normal air environments. Therefore, the rational design of amide-based electrolytes and cell structures, considering evaporation behavior in open-cell systems, is urgently needed.

This study investigates electrolytes based on seven amide solvents with different vapor pressures: *N*,*N*-dimethylformamide (DMF), *N*,*N*-dimethylacetamide (DMA), *N*,*N*-diethylacetamide (DEA), *N*-methylpyrrolidone (NMP), *N*-ethylpyrrolidone (NEP), *N*-methylpiperidone (NMPi), and *N*-methylcaprolactam (NMC) (**Figure 1**). The discharge–charge cycle behaviors of cells with these amide-based electrolytes were examined. These electrolytes were incorporated into a stack-type LAB cell, a semi-open cell system that enables integration into a large-capacity battery cell.[2,3] This setup simulated solvent evaporation during the discharge–charge cycle operation. A gravimetric analysis system, which records continuous weight changes during battery operation,[26] showed that electrolyte evaporation is correlated with the vapor pressure of each solvent. While the weight during discharge/charge confirmed the $2e^-/O_2$ oxygen reduction/evolution reactions (ORR/OER) across all amide-based electrolyte cells, high-viscosity amide electrolytes like NMC-based electrolytes exhibited poor cycling performance due to excessively high overpotentials. In contrast, low-viscosity electrolytes, such as DMA-based electrolytes, performed poorly as well due to their high vapor pressures, which led to fast electrolyte dissipation. However, under high-rate cycling conditions, the issue of electrolyte volatilization is minimized. The open-cell structure also helps mitigate the evaporation issue. The DEA-based electrolyte strikes an optimal balance between viscosity and evaporation, demonstrating superior cyclability at high-rate cycle conditions of 0.8 mA cm^{-2} or more. In contrast, cells with TEG-based electrolytes failed to complete discharge–charge cycles, highlighting the advantages of low-viscosity amide-based electrolytes for high-current operations. Scanning electron microscopy (SEM) and X-ray diffraction (XRD) analyses of cathodes after discharge revealed that high-rate conditions altered the discharge product morphology, forming a film-like structure that enhanced the rechargeability of the amide-based electrolyte cells. These findings contribute to the development of high-power and high-energy rechargeable LABs.

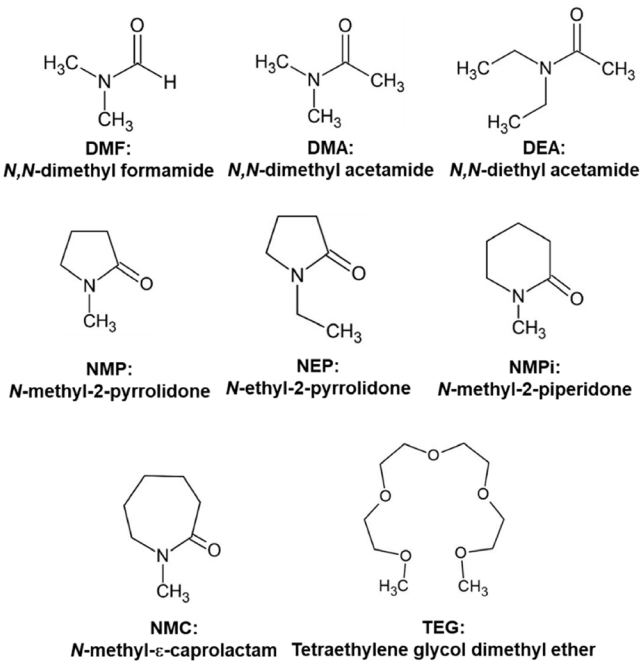

Figure 1. Chemical structure of amides and TEG used as electrolyte solvents in this study.

2. Results and Discussion

2.1. Electrolyte Solvent

To investigate the discharge–charge cycle behavior of the LAB cells in an open system, seven amides with varying viscosities and boiling points were used as electrolyte solvents (Figure 1). TEG was also employed as a conventional LAB electrolyte solvent used elsewhere.[3–13] The vapor pressure of liquid solvents is typically measured by determining the gas-phase pressure in a hermetically sealed chamber (static method).[27] However, solvents with low vapor pressures, especially TEG with its extremely low volatility, are difficult to measure using this approach. To more accurately assess the low vapor pressures of various electrolyte solvents, the vaporization rate was measured directly by monitoring the continuous weight loss of a stainless-steel dish containing

the liquid sample (Figure S2, Supporting Information). These data were then used in the Hertz–Knudsen equation.

$$\pi = Ar_v(2\pi RT/M_w)^{1/2} \quad (1)$$

where P is the vapor pressure, A is a constant, r_v is the vaporization rate per unit area, M_w is the solvent's molecular weight, R is the gas constant, and T is the absolute temperature.[28] The constant A was adjusted to yield a value of $P = 19.8$ mm Hg for deionized water at room temperature (22 °C).[29] This method simplifies the "transpiration method" typically used for materials with low vapor pressures, where volatilization speed is measured with a thermogravimetric apparatus to determine vapor pressure.[30] The measured P values, along with the M_w and viscosity (η) values, are listed in **Table 1**. As expected, solvents with higher boiling points showed lower P. The value for TEG (1.5×10^{-3} mmHg) closely matches the catalog value of 0.25 Pa (1.9×10^{-3} mmHg) at 25 °C, confirming the validity of the vapor pressure measurement in this study.

The highest occupied molecular orbital and the lowest unoccupied molecular orbital (HOMO-LUMO) levels of each solvent molecules were calculated to assess the redox stability of the electrolyte solvents, as summarized in **Figure 2**a. The results indicate that the TEG solvent exhibits good redox stability, with a wider energy gap than compared to the other amides. The higher HOMO levels of amides suggest instability against larger overpotential during charging, while their lower LUMO levels indicate poor reductive tolerance. Both negatively affect the cycle performance when amides are used as LAB electrolyte solvents. However, amide-based electrolytes offer superior cycle performances under high-rate conditions, as discussed later. Figure 2b presents an electrostatic potential map showing the size and charge distribution of each solvent molecule. Larger molecules induce higher viscosities, consistent with the viscosity data in Table 1. The higher viscosity of DMF (0.94 mPa·s) than DMA (0.92 mPa·s), despite DMF having a smaller M_w, can be attributed to greater polarization and stronger molecular interaction, namely, hydrogen bonding. Similarly, TEG has a lower viscosity (3.25 mPa·s) than NMC (5.10 mPa·s), despite TEG having nearly twice the M_w of NMC due to the lower polarization of the TEG molecule. The straight-chain structure of TEG can also contribute to its relatively low viscosity, resulting from its shear-thinning behavior. However, the significantly higher viscosity of TEG solvents compared to low M_w amides limits high-power performance in LABs, as discussed later.

Table 1. Characteristics of the electrolyte solvents.

Solvents	Molecular weight, Mw/g mol^{-1}	Boiling point/ °C[a)]	Viscosity, η/mPa s	Vapor pressure, P/mmHg[c)]
DMF	73.1	153	0.94	3.5
DMA	87.1	165	0.92	1.8
DEA	115.2	185	1.34	6.4×10^{-1}
NMP	99.1	202	1.63	3.4×10^{-1}
NEP	113.2	218	1.87	2.0×10^{-1}
NMPi	113.2	250	2.87	1.3×10^{-1}
NMC	127.2	108[b)]	5.10	7.2×10^{-2}
TEG	222.3	275	3.25	1.5×10^{-3}

[a)]Catalogue values; [b)]Boiling point at 6 mm Hg; [c)]Estimated by measuring the volatilization rate of each solvent (Figure S2, Supporting Information).

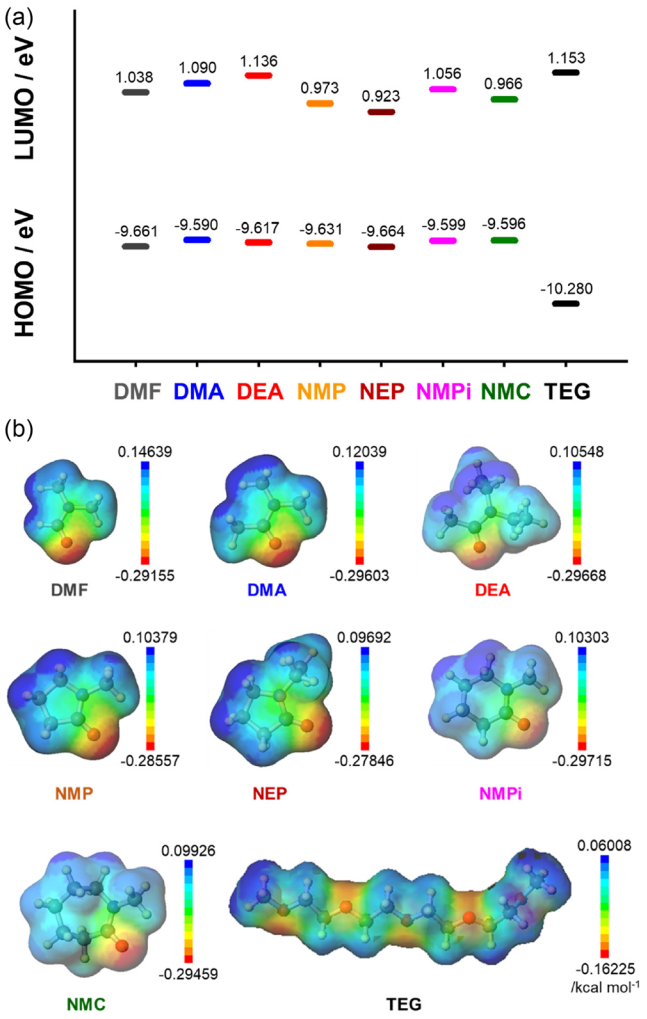

Figure 2. HOMO–LUMO levels a) and electrostatic potential mapping b) of the solvent molecules in this study.

In amide solvents, $LiNO_3$ or $LiNO_2$ were dissolved as supporting salts. Amides are generally unstable with lithium anodes due to their low LUMO levels and lack of reductive tolerance. However, $LiNO_3$ and $LiNO_2$ salts enable the use of amides as LAB electrolyte solvents by forming a thin Li_2O layer on the lithium anode, acting as a high-quality SEI and preventing amide reduction.[20,22,31,32] The NO_3^- anion in $LiNO_3$ salt electrolytes passivates the Li surface ($NO_3^- + 2Li \rightarrow NO_2^- + Li_2O$), preventing direct contact between amide molecules and Li. The Li_2O layer produced by the NO_3^- under oxygen atomosphere is quite thin and uniform, successfully preventing needle-like dendrite growth and surface lithium pulverization throughout the lithium dissolution/deposition cycles.[31,32] The consumed NO_3^- anion can be regenerated in an oxygen atmosphere ($NO_2^- + 1/2O_2 \rightarrow NO_3^-$). In $LiNO_2$ salt electrolytes under oxygen, the NO_3^-

anion, which coexists with NO_2^-, also contributes to the formation of a thin Li_2O layer, making amides compatible as LAB electrolyte solvents. The ionic conductivities and viscosities of the prepared electrolytes are listed in Table S1, Supporting Information. Dissolving $LiNO_3$ and $LiNO_2$ salts increases solvent viscosity due to enhanced molecular interactions between the solvent and dissociated salt. This effect is more pronounced for $LiNO_3$, which has a higher solvation energy and undergoes greater ionic dissociation than $LiNO_2$.[22] The Walden plot of the prepared electrolytes (Figure S3, Supporting Information) shows almost identical salt dissociation degrees across all amide solvents, but TEG exhibited an ionic conductivity one order of magnitude lower than that of NMC- or NMPi-based electrolytes. Due to the lower salt dissociation in TEG, LAB cells with TEG-NO_3 and TEG-NO_2 electrolytes failed to show discharge–charge behavior under the tested cycle conditions. Therefore, TEG-TFSI, a conventional electrolyte used in many LAB studies,[3–13] was employed instead.

2.2. Cycle Performance

Discharge–charge cycle experiments were conducted on LAB cells with amide-based electrolytes. Stack-type LAB cells were employed (see schematic Figure S1, Supporting Information), where oxygen gas is exchanged through the gas diffusion layer (GDL) cross-section rather than from the plane surface. This design enables multiple electrode stackings, achieving Ah-class cell capacities while ensuring an efficient oxygen flow path during discharge and charge.[2,3] A highly porous, high surface area carbon nanotubes (CNT) sheet (Brunauer–Emmett–Teller (BET) surface area of 910 $m^2\ g^{-1}$) was used as the cathode to achieve high-rate performance.[12] However, the semi-open-cell structure inevitably allows some electrolyte evaporation, which becomes more prominent with high P solvent electrolytes. **Figure 3**a,b shows the voltage profiles of LAB cells with DMA-, DEA-, and NMC-based electrolytes, along with the cell weight change (W) profiles (results for other amide-based electrolyte cells are

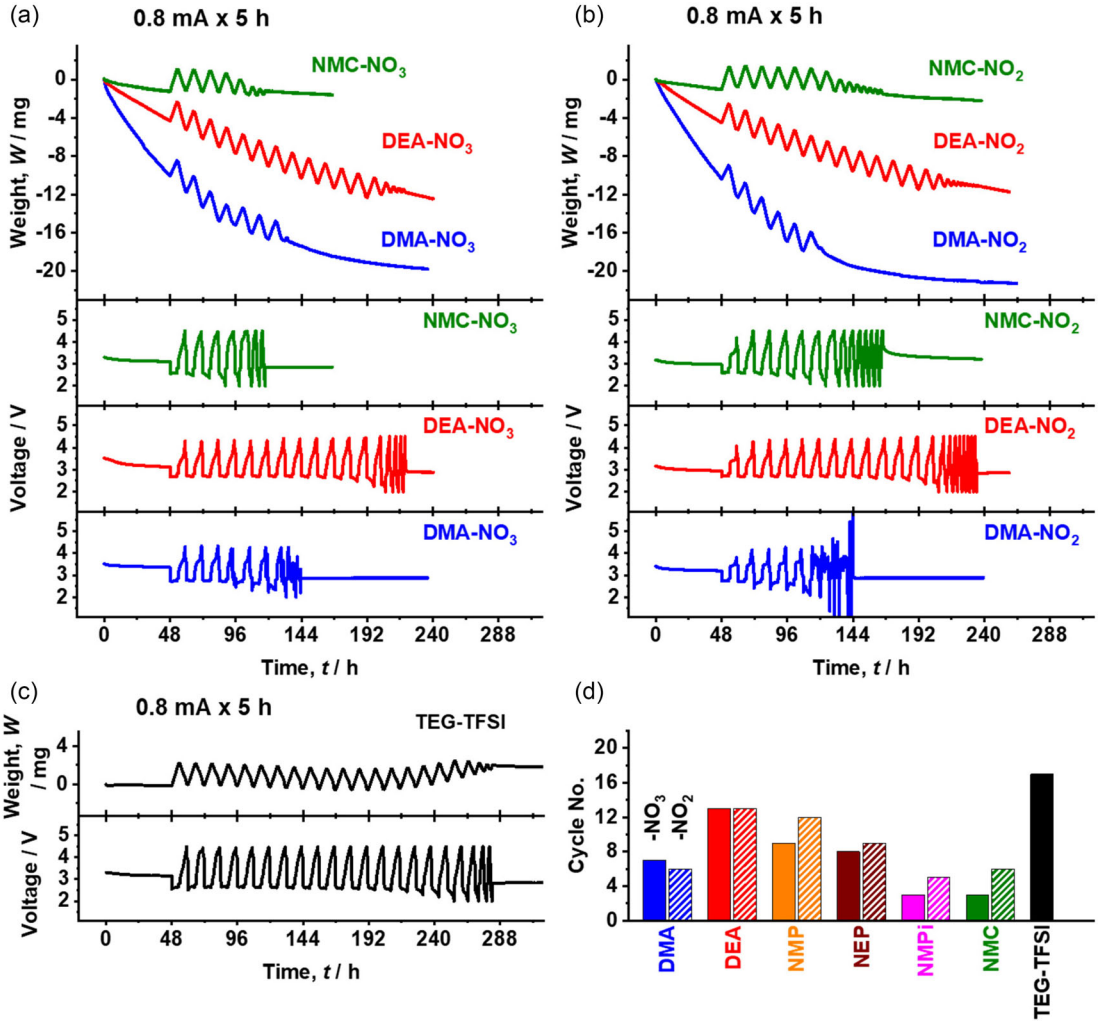

Figure 3. a-c) Cell weight change, W, and voltage profiles of the LAB cells of DMA-, DEA-, NMC-, and TEG-based electrolytes. Additional W and voltage profiles were shown in Supporting Information (Figure S4). d) Cycle number of the LAB cells under the cycle condition of 0.8 mA × 5 h discharges and charges.

in Figure S4, Supporting Information). A 48-hour rest period was applied before the 0.8 mA × 5 h discharge–charge cycles to fully equilibrate the cells with the oxygen environment. The *W* profiles in Figure 3 present continuous weight loss immediately after cell assembly ($t = 0$ h) due to electrolyte solvent evaporation, along with the weight changes observed during ORR/OER in discharge/charge cycles. The weight loss due to solvent evaporation followed the order of the solvent's boiling point and was thus related to the solvent *P* magnitude. Due to the rapid electrolyte dissipation, the cells with DMF-based electrolytes could not complete discharge–charge cycles (Figure S4, Supporting Information). The voltage fluctuation in DMF electrolyte cells after ≈24 h indicates the loss of cell contact due to significant DMF solvent evaporation and alterations in electrolyte composition.

The cells with DMA-based electrolytes, which exhibited the next fastest evaporation, were able to perform discharge–charge cycles. However, these cells showed voltage drops after the 4th or 5th charge, likely due to internal short circuits. This behavior is commonly observed in lean electrolyte conditions, where inhomogeneous lithium plating leads to Li dendrite growth and micro-short circuits.[24] As a result of charging failures, DMA-based electrolyte cells had a short cycle life of approximately six cycles. In contrast, the *W* profiles demonstrate successful suppression of electrolyte evaporation in NMC-based electrolyte cells. However, high overpotentials during both discharging and charging limited the number of cycles to 3–6. The high viscosity of NMC-based electrolytes hinders smooth oxygen diffusion and Li^+ transfer, increasing overpotentials and causing battery material deterioration, which leads to rapid loss of rechargeability. In addition, the high-viscosity electrolytes may poorly wet the cathode pores, which could also contribute to the short cycle life. However, this was not the case because the cell capacitance immediately after the cell assembly (0.15 F, Figure S5, Supporting Information) was close to that of the CNT-based cathode (0.16 F, 40 F g^{-1} per CNT weight[12]), suggesting that the electrolyte had fully wetted the electrolyte. The balance between solvent volatility, which causes cell contact loss, and solvent viscosity, which impedes reactant supply, makes DEA-based electrolytes the most efficient for LABs, enabling 13-cycle runs in the stack-type LAB cell system. The DEA-based electrolyte cell was also able to run even under a dry air condition with a dew point of −60 to −50 °C, demonstrating the same evaporation behavior and cycle number as that under pure oxygen condition (Figure S6, Supporting Information). This result positively suggests that the cell system can be applied to develop "true" LABs that can be used in atmospheric air. Although the atmospheric oxygen concentration (≈21%) slightly reduces the discharge voltage, the decay calculates the energy density loss of no more than 4%. The same cycle number indicates that the charge failure due to the electrolyte dissipation limits the cycle life. Though, the cycle life was shorter than that of the TEG-TFSI cell (Figure 3c), which achieved 17 cycles and demonstrated the most successful evaporation suppression.

Many studies have reported LAB cells achieving over a hundred cycles with TEG-based electrolytes.[33–35] However, most of these cycles do not meet the practical energy requirements of modern batteries. The cycle condition we investigated here (0.8 mA × 5 h) delivers an energy density of ≈150 Wh kg^{-1} to the stack-type LAB cell (≈70 mg). This condition can be considered a minimum benchmark for surpassing the current LiB technology, which offers an energy density of 100-200 Wh kg^{-1}.[36] In this context, the TEG-TFSI electrolyte cell, which achieves 17 cycles, demonstrates competitive performance compared to previous high-energy-density LAB reports,[2–4] though extending its cycle life remains a significant challenge. Figure 3d summarizes the cycling performance of stack-type LAB cells, showing that DEA-based electrolyte cells exhibit the best cyclability among amide-based electrolytes. The graph also highlights the superior cyclability of the $LiNO_2$ salt electrolytes, which achieve ≈4 more cycles than $LiNO_3$ salt electrolyte cells. This improved performance is attributed to the redox mediator (RM) effect of the NO_2^- anion.[22] During charging, the NO_2^- anion is oxidized to NO_2 at a redox potential of 3.5 V ($NO_2^- \rightarrow NO_2 + e^-$, 3.5 V vs Li/Li^+), prior to the direct oxidation of Li_2O_2 ($Li_2O_2 \rightarrow 2Li^+ + O_2 + 2e^-$). The NO_2 molecule then chemically oxidizes the Li_2O_2 discharge product, reducing itself back to NO_2^- ($Li_2O_2 + 2NO_2 \rightarrow 2Li^+ + O_2 + 2NO_2^-$). This reaction prevents the charging voltage from exceeding the NO_2^- redox potential (3.5 V), thus avoiding the oxidative decomposition of battery materials and extending the cycle life of LAB cells. These results highlight the advantages of using $LiNO_2$ as an electrolyte supporting salt with RM functionality.

The observed decrease in *W* throughout the battery test indicates an increase in salt concentration due to solvent dissipation, which decreases the electrolyte vapor pressure according to Raoult's law. This behavior is more pronounced in high *P* solvent electrolytes, such as DMF- or DMA-based electrolytes, and is particularly evident in $LiNO_2$ salt electrolytes than in the $LiNO_3$ electrolyte. This is because $LiNO_2$ has a lower solvation energy than $LiNO_3$.[22] Although both salts are fully dissolved in amide solvents at 1.0 M, the lower dissociation degree of $LiNO_2$ results in higher volatility compared to $LiNO_3$ electrolytes dissolved in the same solvent. To investigate the evaporation behavior of the stack-type LAB cells, the evaporation rate (r_{evap}) was determined from the slope of the *W* profile immediately before the start of the discharge–charge cycle ($t = 48$ h). For the high *P* solvent electrolytes (DMF-, DMA-, and DEA-based electrolyte cells), the r_{evap} was derived from the slope of the *W* profile at $W = -3.2$ mg, corresponding to the 10 wt% decrease in electrolyte solvent. This adjustment eliminates the influence of salt condensation and ensures a fair evaluation of the evaporation behavior. The obtained r_{evap} values are plotted in **Figure 4** against the $PM_w^{1/2}$ of each solvent, which correlates with the pure solvent volatilization rate (r_v) measured previously (Figure S2, Supporting Information). The graph shows a nonlinear relationship between r_{evap} and $PM_w^{1/2}$ (or r_v), expressed as.

$$r_{evap} \propto (PM_w^{1/2})^{\alpha} \quad (2)$$

where α is 0.62, derived from the linear fitting of the data points (black dotted line). An α value less than one indicates that the cell geometry and the small pores in the cathode/separator impede solvent evaporation,[37] suggesting that electrolyte retention can be enhanced by optimizing cell structures and cathode pore architectures. For instance, applying a wrap film with a 1 mm pinhole to a stainless-steel cathode cell with perforated holes significantly suppressed r_{evap}, yielding an α value of 0.49 (gray dotted line).

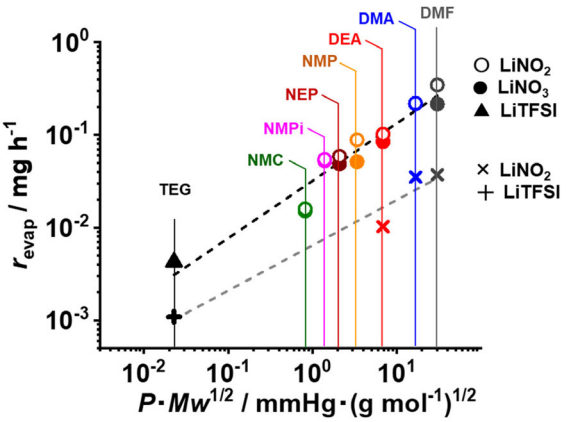

Figure 4. Evaporation rate of the electrolyte solvents from the LAB cells (r_{evap}) plotted against the $PM_w^{1/2}$ value of each electrolyte solvent. The filled and open circles represent the data points for $LiNO_3$ and $LiNO_2$ salt electrolytes, respectively. The black-filled triangle shows the data point for TEG-TFSI electrolyte. The black dotted line represents the linear fitting of the data points, deriving 0.62 as the slope of the line, α. The × and + symbols denote the r_{evap} for, DMF-NO_2, DMA-NO_2, DEA-NO_2 (×), and TEG-TFSI (+) electrolyte cells with a pinhole wrap film, providing a linear fitting line (gray dotted line) with a slope of $\alpha = 0.49$.

Interestingly, wrapping with a pinhole significantly extended the cycle life of the high P amide electrolyte cell (Figure S7, Supporting Information). The DMA-NO_2 and DEA-NO_2 cells, which completed 6 and 13 cycles in Figure 2, respectively, increased to 26 and 18 cycles when a pinhole wrap was applied to the cathode case lid. In contrast, the wrapping had minimal impact on the cyclability of the TEG-TFSI cell, suggesting that evaporation was not a problem for the TEG-based electrolyte. However, the intrinsic instability of the TEG electrolyte limits its cyclability, as previously reported.[16] The DMF-NO_2 cell, even with a pinhole wrap, failed to function. While DMF-based electrolytes are known to enable rechargeability in LABs,[38] their relatively fast oxidative decomposition likely rendered the DMF electrolyte nonfunctional after an initial 48-hour rest period. During this period, the DMF-NO_3 and DMF-NO_2 cells voltage quickly dropped to 2.8 V within ≈5 h of assembling (Figure S4 and S7, Supporting Information), indicating self-discharge due to the spontaneous oxidation of DMF. It should be also noted that hermetically sealed LAB cells with no headspace could not discharge because they could not intake oxygen. This highlights the challenge of packaging cells to prevent electrolyte evaporation while ensuring adequate oxygen inhalation and exhalation for large-capacity battery integration.

The weight changes of cells during discharge and charge represent the ORR/OER process in LAB. The time derivatives of W (dW/dt) were derived, with profiles shown in **Figure 5**a for the first three cycles of cells with TEG-TFSI, DEA-NO_3, and DEA-NO_2 electrolyte (profiles for other electrolyte cells are in Figure S8, Supporting Information). The r_{evap} values were deducted from dW/dt to evaluate discharge and charge behavior without considering solvent evaporation. The dW/dt profiles follow the red dotted lines (+0.478 mg h^{-1}) during discharge at an applied current of 0.8 mA, accurately representing the $2e^-/O_2$ ORR process of LAB ($2Li^+ + O_2 + 2e^- \rightarrow Li_2O_2$). The charging behavior, however, varies with electrolyte solvent and salt. First, the TEG-TFSI electrolyte cell showed a decrease in gas evolution

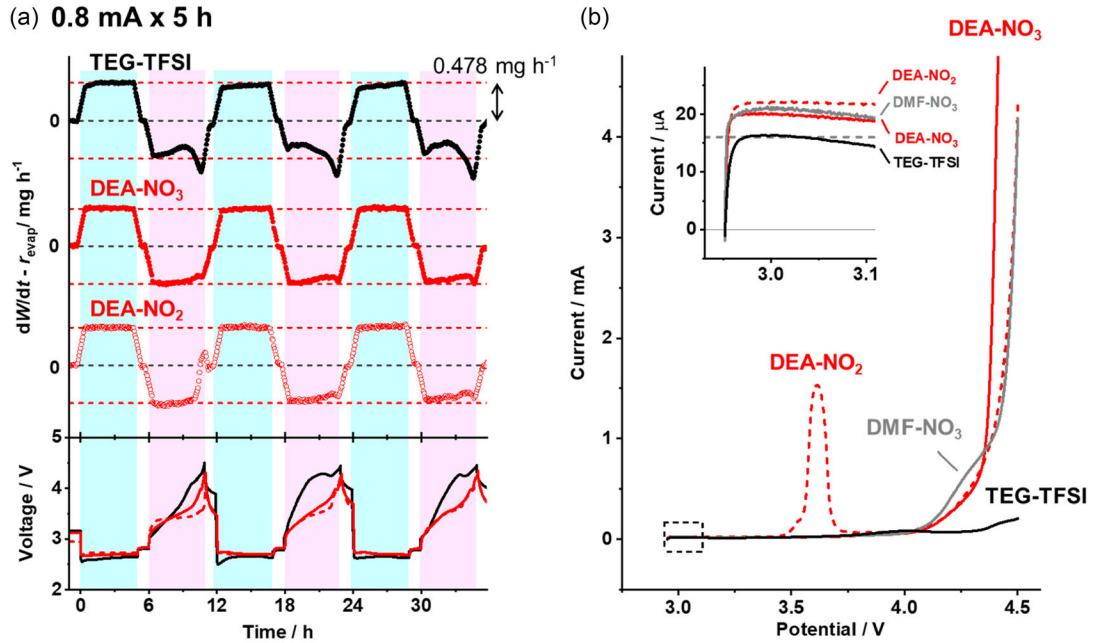

Figure 5. a) The dW/dt-r_{evap} and voltage profiles of TEG-TFSI (black, filled circle), DEA-NO_3 (red, filled circle), and DEA-NO_2 (red, open circle) electrolyte cells for the first three cycle runs. The profiles were derived from the weight profiles shown in Figure 3. The pale blue and red boxes show the regions of discharge and charge, respectively. The red dotted lines in the dW/dt-r_{evap} profiles show the weight increase/decrease rates by $2e^-/O_2$ ORR/OER (±0.478 mg h^{-1} at 0.8 mA). b) LSV anodic scan profiles of TEG-TFSI (black straight line), DEA-NO_3 (red straight line), DEA-NO_2 (red dotted line), and DMF-NO_3 (gray straight line) electrolyte cells from 2.95 V to 4.50 V. The superimposed shows the enlarged profiles of the dotted square region.

midway through charging (≈8, ≈20, and ≈32 h), then exceeded the $2e^-/O_2$ OER line ($-0.478\ mg\ h^{-1}$) toward the end of the charge (≈10, ≈22, and ≈34 h). This is attributed to a decrease in O_2 evolution, followed by CO_2 evolution with the charge, indicating incomplete O_2 recovery in TEG-based electrolyte cells, as confirmed by online differential electrochemical mass spectrometry (DEMS).[26] Conversely, the DEA-NO_3 electrolyte cell followed the $2e^-/O_2$ OER line ($-0.478\ mg\ h^{-1}$), indicating improved O_2 evolution and reduced CO_2 evolution. This demonstrates the improved rechargeability of the DEA-based electrolyte, providing better stability against attack by active oxygen species. However, the dW/dt profile of the DEA-NO_3 cell showed signs of CO_2 evolution at the end of the second or third charge (≈22 and ≈34 h), suggesting limited stability against active oxygen. The dW/dt profile of the DEA-NO_2 cell closely mirrored that of the DEA-NO_3 cell but showed an earlier reduction in O_2 evolution near the end of the first charging cycle (≈10 h). This indicates the oxidation of the NO_2^- anion to the NO_3^- anion ($NO_2^- + 1/2O_2 \rightarrow NO_3^-$), likely accelerated in the highly oxidative environment during charging. The O_2 evolved from Li_2O_2 oxidation may have partly been consumed in the oxidation of NO_2^- anion. Although NO_2^- is the primary anion in $LiNO_2$ electrolyte, ion chromatographic analysis revealed that the NO_3^- anion became dominant after several discharge–charge cycles, finally being the same NO_2^-/NO_3^- anion composition with $LiNO_3$ salt electrolyte.[22] The conversion of NO_2^- to NO_3^- is further supported by the disappearance of the RM effect of the NO_2^- anion. The DEA-NO_2 electrolyte cell exhibited a charging voltage plateau of ≈3.5 V during the first charge, but this plateau vanished by the 3rd or 4th charge, following the same voltage profile as the DEA-NO_3 cell. This explains the longer cycle life of $LiNO_2$ salt electrolyte cells compared to $LiNO_3$ cells. Increasing the NO_2^- anion concentration and suppressing the NO_2^- to NO_3^- conversion could enhance cyclability in the $LiNO_2$ salt electrolyte cells.

The oxidative degradation of LAB electrolytes results from two primary factors: active oxygen attack on the electrolyte molecules and electrochemical oxidation within the charging potential window. During the charging process, excess active oxygen produced by Li_2O_2 oxidation deteriorates both the electrolytes and electrodes, particularly in TEG-based electrolyte cells that cause intense CO_2 evolution. The oxygen radical attacks the glyme chain carbon to form alkyl peroxides, which undergo a cascade reaction analogous to combustion to eventually produce CO_2, H_2O, and carbonates.[39] A similar oxidation mechanism has been proposed for amide molecules by the oxygen radical attacking the carbonyl carbon or alkyl carbons adjacent to the nitrogen, but the higher activation energy and free energy than that of glyme indicate the greater tolerance of amides to active oxygen attack.[40,41] Instead, the higher HOMO levels of the amides pose oxidative instability by the high-voltage electrode. To distinguish between these oxidation factors, linear sweep voltammetry (LSV) anodic scans were performed on amide- and TEG-based electrolyte cells after assembly. The scan profiles, as shown in Figure 5b, reveal a sharp increase in oxidation currents at >4.1 V for the DEA-NO_3, DEA-NO_2, and DMF-NO_3 cells, while the TEG-TFSI cell shows a minor oxidation current at >4.3 V. These results align with the expected oxidative stabilities, as indicated by the HOMO levels of the amides and TEG in Figure 2a. The intense oxidation current peak at 3.6 V for the DEA-NO_2 cell is attributed to the oxidation of NO_2^- anion to NO_2 ($NO_2^- \rightarrow NO_2 + e^-$), with a conversion yield of 46% from the peak area capacity (1.4 C). As the cells contained no discharge product (Li_2O_2) to decompose, the oxidation currents stem from the electrochemical conversion of the electrolytes. LSV profiles indicated that the enhanced rechargeability of the amide-based electrolyte cells results from their improved stability against active oxygens attack. These low-viscosity amide electrolytes enable LAB cells to charge with suppressed overpotentials by promoting efficient oxygen and Li^+ transport, thus enhancing rechargeability. However, amide-based electrolyte cells experience rapid loss of cyclability once the charging voltage exceeds 4.1 V due to the lack of electrochemical oxidation stability. In fact, amide electrolyte cells undergo oxidative decomposition even at the beginning of the anodic scan. The enlarged scan profiles in Figure 5b show an oxidation current of ≈21 μA for the amide-based electrolyte cells, higher than the 16 μA observed for the TEG-TFSI cell. Given that the $0.1\ mV\ s^{-1}$ scan rate for cells with a CNT sheet cathode (0.16 F, $40\ F\ g^{-1}$ per CNT weight[12]) produces a capacitor current of 16 μA (gray dotted line), the enlarged profile confirms that the TEG-TFSI cell does not undergo oxidative decomposition near the open-circuit voltage (OCV). In contrast, the amide electrolytes undergo electrochemical oxidation of ≈5 μA. This spontaneous oxidation of amide-based electrolytes contributes to voltage decay during the initial 48-hour rest period, particularly for the DMF-based electrolyte cells, which exhibit the highest fluidity (or the lowest viscosity) among the electrolytes studied here.

2.3. Cycle Performance at High Current Rates

The cycle test on the LAB stack cells demonstrated the superiority of TEG-TFSI as an LAB electrolyte. However, the dW/dt profile suggests limited stability against oxidative degradation. Among amide-based electrolytes, DEA-NO_2 exhibits the best cyclability due to its low solvent viscosity and minimal solvent dissipation during cycling. Additionally, the RM effect of the NO_2^- anion further enhances cyclability. Although the cycle condition current rate of 0.8 mA ($0.4\ mA\ cm^{-2}$ per electrode area) exceeds that of LAB studies reported elsewhere,[33–35] it still fails to meet the practical battery power requirements. The cell mass of ≈70 mg, which can be reduced to ≈40 mg by using a thinner Li foil anode and the decreasing electrolyte volume, barely achieves a power density of $50\ W\ kg^{-1}$ at 0.8 mA. This is significantly lower than the $>10^3\ W\ kg^{-1}$ delivered by LiB technology.[36] Improving power performance is a critical challenge for LAB, prompting further investigation into cycle performance at higher current rates.

Figure 6a,b presents the W and voltage profiles of the DEA-NO_2 and TEG-TFSI cells at current rates of 1.6, 2.4, and 3.2 mA (0.8, 1.2, and $1.6\ mA\ cm^{-2}$ per electrode area, respectively) with a fixed capacity of 4 mAh ($2\ mAh\ cm^{-2}$). The initial rest time before the cycling experiment was reduced to 12 h to retain as much electrolyte as possible. Figure 6c summarizes the number of cycles achieved at each cycle rate. When the current rate was increased to 1.6 mA, the DEA-NO_2 cell achieved 17 cycles, demonstrating improved cyclability under high-rate conditions in the shorter experimental times. This improvement is attributed to the high-rate capability of low-viscosity amide electrolytes, which reduce internal resistance by enhancing oxygen

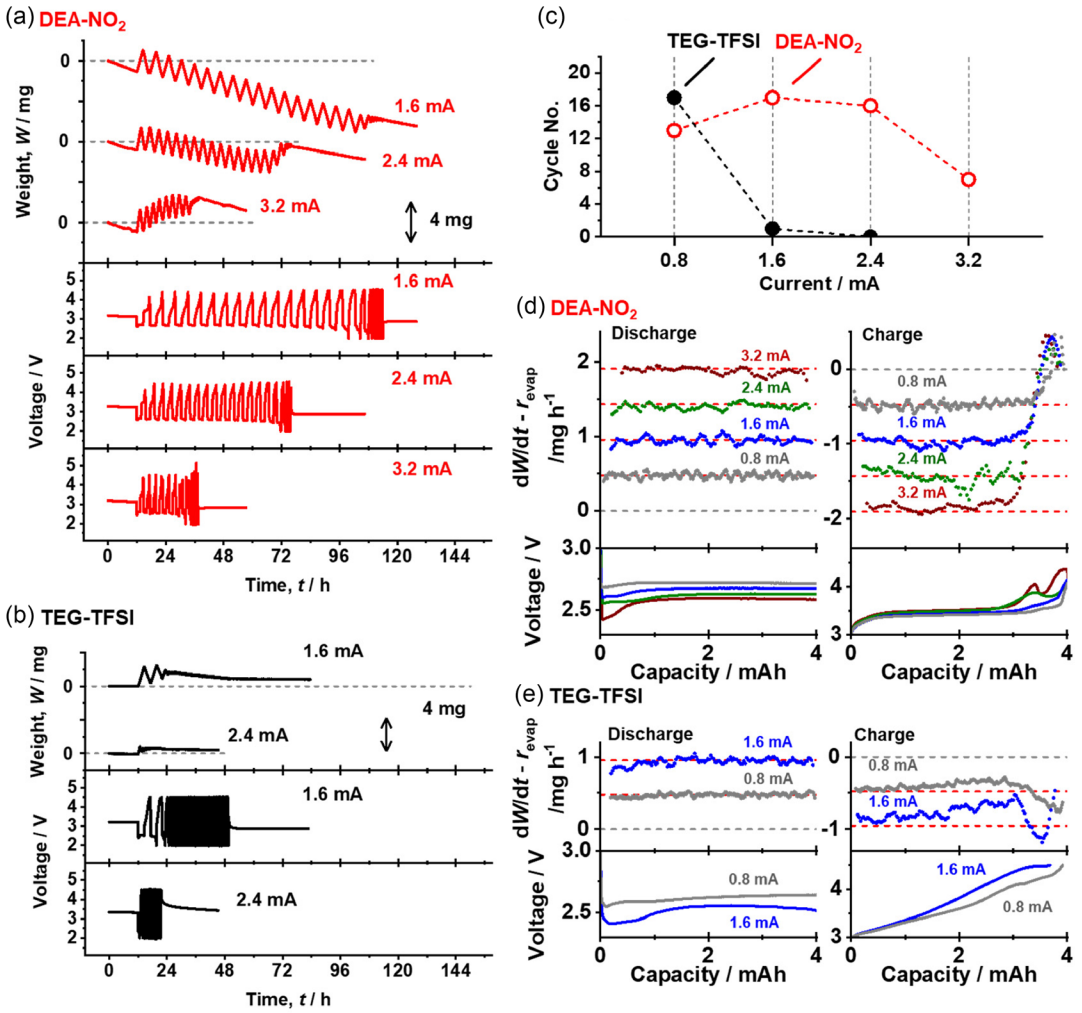

Figure 6. a,b) Cell weight change, W, and voltage profiles of the DEA-NO_2 (a) and TEG-TFSI (b) electrolyte cells at the cycle conditions of 1.6, 2.4, and 3.2 mA (0.8, 1.2, and 1.6 mA cm^{-2}) current rates. The cycle capacity was fixed to 4.0 mAh (2.0 mAh cm^{-2}). c) Cycle number of the LAB cells at different current rates of 0.8, 1.6, 2.4, and 3.2 mA (0.4, 0.8, 1.2, and 1.6 mA cm^{-2}). d,e) The dW/dt-r_{evap} and voltage profiles of DEA-NO_2 (d) and TEG-TFSI (e) electrolyte cells for the first cycle runs. The red dotted lines in the dW/dt-r_{evap} profiles represent the weight increase/decrease by $2e^-/O_2$ ORR/OER at each current rate.

diffusion, thus enabling discharge at high current.[15] The DEA-NO_2 cell was rechargeable at a rate of 2.4 mA for 16 cycles. However, at 3.2 mA, the cycle number decreased to six, with increasing W behavior during the cycle test, indicating charging failure. The cell reached the cutoff voltage of 4.5 V before fully charging, and DEA-based electrolytes undergo significant oxidation at voltages >4.1 V, accelerating cell degradation. Reducing the charge current rate only will improve cyclability, even under the high-rate cycling conditions. The high-rate cycling experiment also revealed the TEG-TFSI electrolyte limitations. The TEG-TFSI cell exhibited only one cycle at 1.6 mA (0.8 mA cm^{-2}) and failed to operate at 2.4 mA (1.2 mA cm^{-2}), indicating its suitability only for extremely low-power devices.

Figure 6d,e shows the dW/dt profiles for the DEA-NO_2 and TEG-TFSI cells during their first discharge and charge cycles. The DEA-NO_2 cells follow the $2e^-/O_2$ lines (red dotted lines), indicating ideal ORR/OER at all cycling current rates. The decrease in gas evolution after a charge of ≈3 mAh represents the NO_2^- anion oxidation to NO_3^-, as previously discussed. In contrast, the TEG-TFSI cell fails to maintain a stable discharge voltage plateau at 1.6 mA (0.8 mA cm^{-2}), and its dW/dt profile during charging indicates insufficient oxygen evolution. This is attributed to the high viscosity of the TEG-TFSI electrolyte, which hinders smooth oxygen exchange. These results confirm that low-viscosity amide-based electrolytes are essential for high-power rechargeable LABs. However, their volatility poses a challenge for cell packaging. It is crucial to maintain fast oxygen flow while suppressing electrolyte dissipation. Although volatilization can be suppressed by gelling the liquid electrolyte or replacing it with solid Li^+-conductive electrolytes,[42–44] achieving high current rate capability remains difficult. Because the cell's geometric design plays an important role in electrolyte retention, studying the gas flow around the cell structure would provide a new strategy for developing high-power, long-life rechargeable LABs.

To further investigate the mechanism behind high-rate cyclability, the discharge products deposited on the CNT cathode were analyzed. **Figure 7** a,b shows SEM images of the cathodes after an 8 mAh (4 mAh cm^{-2}) discharge in DEA-NO_2 cells under low- (0.4 mA (a)) and high-rate (2.4 mA (b)) conditions. The corresponding energy-dispersive spectroscopy (EDS) oxygen (O) elemental maps are superimposed on the SEM images (additional SEM images at different magnifications are shown in Figure S9, Supporting Information). Under the low-rate condition (a), discrete particles, ≈200 nm in diameter, precipitated on the CNT bundles, which were covered with O. This suggests two pathways for discharge product formation, that is, the solution and surface reduction pathways.[45] The ORR in LAB occurs as follows

$$Li^+ + O_2* + e^- \rightarrow LiO_2* \quad (3)$$

$$LiO_2* \rightarrow LiO_2 \quad (4a)$$

$$2LiO_2 \rightarrow Li_2O_2* + O_2 \quad (4b)$$

$$LiO_2* + Li^+ + e^- \rightarrow Li_2O_2* \quad (5)$$

where * denotes the species adsorbed on the cathode surface. First, one-electron oxygen reduction occurs at the cathode surface (3), followed by two pathways. The one-electron reduction intermediate (LiO_2*) is released from the cathode surface (4a) and undergoes disproportionation (4b), forming highly crystalline particles, typically in a toroidal shape, on the cathode surface. This is known as the "solution" pathway. Alternatively, the LiO_2* intermediate remains on the surface, further accepting one-electron reduction (5), forming a thin Li_2O_2 film known as "surface" reduction. The SEM image under the low-rate condition (a) suggests a mixed reduction pathway, forming both discrete particles and thin films with different discharge product morphologies. In contrast, the SEM image under high-rate conditions (b) likely favors surface reduction, as no distinct particles precipitate, and the CNT bundles are uniformly covered with a thin Li_2O_2 film. XRD analysis of the CNT cathodes after discharge (Figure 7c) supports this trend. While both spectra confirm that Li_2O_2 is the main discharge product, the low-rate condition slightly sharpens the Li_2O_2 reflection peaks, indicating higher crystallinity. The low-rate spectrum also shows a small peak at 2thete = 33.5°, between the 100 and 101 reflections of Li_2O_2. Although we could not precisely assign this peak, it suggests partial evolution of the Li_2O 111 reflection, likely due to Li_2O_2 disproportionation ($2Li_2O_2 \rightarrow 2Li_2O + O_2$).[46] Though Li_2O_2 disproportionation typically occurs at >250 °C, trace impurities might promote the reaction even at room temperature.

The morphology of the discharge product influences the rechargeability of the subsequent charge. Figure 7d compares two charge profiles after a 4.0 mAh discharge, with discharge

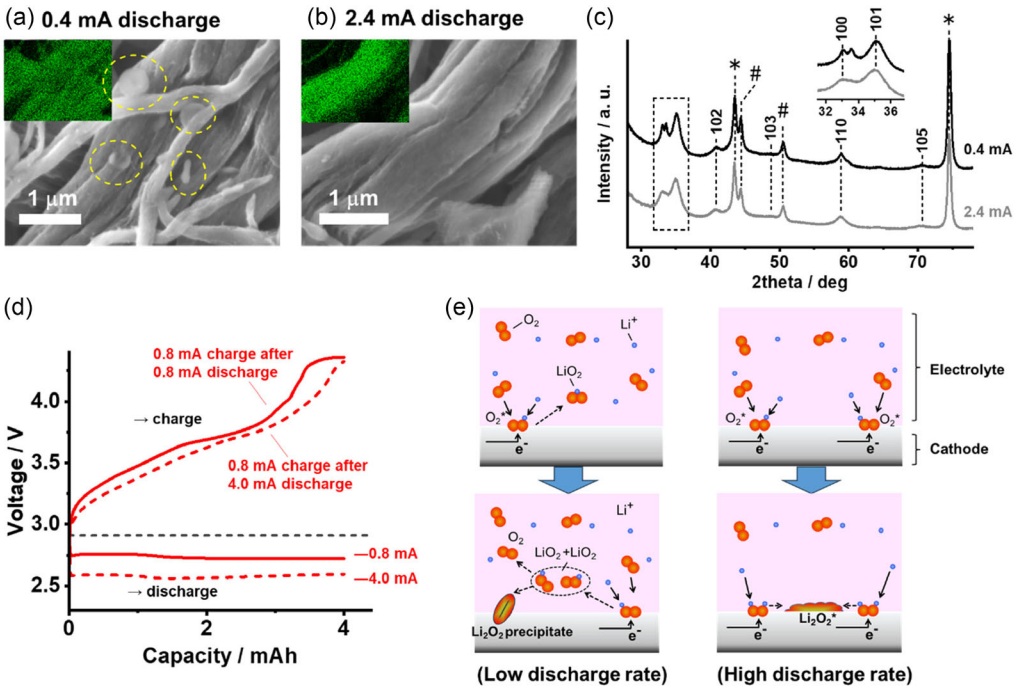

Figure 7. a,b) SEM images of CNT sheet cathodes after 8 mAh (4 mAh cm^{-2}) discharges at discharge rates of 0.4 mA (a) and 2.4 mA (b). The insets show the corresponding EDS oxygen (O) element mappings. The yellow dotted circles in (a) indicate the toroid particles deposition on CNT bundle surface. c) XRD profiles of CNT sheet cathodes after 8 mAh discharges at 0.4 mA (black line) and 2.4 mA (gray line). The inset shows the enlarged XRD profiles of the dotted square region. The numbers in the graph indicate the miller indices for the Li_2O_2 crystal diffraction. The * and # symbols denote the reflections from a stainless-steel plate (sample holder) and GDL, respectively. d) Discharge and charge profiles of LAB cells at a charge rate of 0.8 mA after the 4 mAh (2 mAh cm^{-2}) discharges at 0.8 mA (solid red line) and 4.0 mA (dotted red line). The electrolyte was 1.0 M $LiNO_3$ dissolved in an equal volume mixture of DEA and DMA. e) Schematic illustrations of ORR near the carbon cathode surface at low (left) and high (right) discharge current rates. The low discharge rate rather produces Li_2O_2 solid particles due to the slow ORR kinetics allowing free LiO_2 and its disproportionation, while the high discharge rate tends to produce surface filmy Li_2O_2 deposit due to the fast ORR.

rates of 0.8 mA and 4.0 mA, while the charge rate remained fixed at 0.8 mA. $LiNO_3$ salt was used to minimize the RM effect and compare charge behavior, while DMA was added to the DEA solvent to reduce internal resistance and facilitate a high discharge rate of 4.0 mA (2.0 mA cm^{-2}). The cells discharged at both 0.8 mA and 4.0 mA current rates, maintaining stable voltage plateaus of 2.75 V and 2.60 V, respectively. Although the charge rate was constant, the cell discharging at 4.0 mA exhibited a lower charge voltage throughout the charging process, indicating improved rechargeability under high-rate discharge. This effect is associated with the formation of highly decomposable Li_2O_2. The charge profile of the low-rate discharge cell exhibited a 4.3 V plateau near the end of the charge (>≈3.5 mAh), indicating that severe electrolyte oxidation occurred in this high-voltage region, as shown in the LSV scan in Figure 5b (>4.1 V). The Li_2O_2 particles deposited during the low-rate discharge should have lost electrical contact without being fully decomposed. Figure 7e illustrates the ORR process under low- and high-rate discharge conditions. At low discharge rates, the solvated LiO_2 intermediate in the electrolyte gradually forms Li_2O_2 particles, however, these particles are less likely to decompose during subsequent charging due to distance from the cathode surface and the high crystallinity. At higher discharge rates, the reduction of LiO_2* occurs at the cathode surface, driven by a relative shortage of surface oxygen to accept cathode electrons. This results in a thinner discharge product, which is more easily decomposed due to increased contact with the cathode surface. Furthermore, although Li_2O_2 is typically insulating, non-crystalline amorphous Li_2O_2 has been shown to be conductive, enhancing rechargeability by improving the electrical conductivity of the discharge product.[47,48] This also accounts for the improved cyclability under high-rate cycling conditions.

The discharge product morphology in LABs can be influenced by factors such as the rate-dependent Li_2O_2 morphology,[49] the acceptor/donor numbers (AN/DN) of the electrolyte,[45] traces of protic solvent molecules,[50] and cathode surface chemistry.[51–54] Amide electrolytes, with approximately twice the DN of TEG,[15] tend to stabilize the LiO_2 intermediate and promote the growth of discrete particles via the solution pathway, in contrast to the TEG-TFSI electrolyte. However, high-rate discharge suppresses the solution pathway and encourages the deposition of Li_2O_2 as a thin film through surface reduction, even in amide electrolytes. Previous studies have suggested that a thin-film discharge product hinders electron transfer and causes premature discharge termination.[55] This, however, is not the case in this study, which uses a highly porous CNT sheet cathode with a high surface area. The CNT cathode offers a large ORR surface and ensures rapid reactant supply, preventing thin-film discharge products from blocking the cathode pores and terminating the reaction. Therefore, a CNT cathode paired with a low-viscosity amide-based electrolyte presents a promising combination for developing high-energy, high-power LABs. However, electrolyte evaporation through the oxygen ventilation path is inevitable, necessitating careful consideration of cell packaging and operating conditions to fully realize the full potential of high-energy-density LABs. This study provides a rational design approach for LAB electrolytes aimed at high-power, rechargeable LABs.

3. Conclusion

To clarify the rational choice of amide-based electrolytes, this study investigated the discharge and charge cycle performance of LAB cells in an open-cell structure. The gravimetric analysis demonstrated the $2e^-/O_2$ ORR/OER across all amide-based electrolyte cells, along with the continuous evaporation behavior of the electrolytes that correlates with the vapor pressure of the electrolyte solvents. The discharge–charge cycle experiment revealed the superior cycle performance of the cells with low-viscosity amide-based electrolytes, such as DEA-NO_2, at high current rates, conditions that cells with TEG-based electrolyte were never able to complete. This is due to the fast oxygen and Li^+ transfer propensity of the low-viscosity amide electrolyte to facilitate high current rate discharge. The study revealed that high-rate condition improves the rechargeability of amide-based electrolyte cells by forming a filmy Li_2O_2 discharge product that is easier to decompose during charging. However, low-viscosity amide electrolyte is highly volatile, thus open-cell structure that ensures rapid oxygen gas supply while suppressing electrolyte evaporation is inevitable to achieve the superior cycle performance at high rates. Developing such open-cell structures and exploring low-viscosity electrolyte with low vapor pressure will improve the cycle performance of LAB, paving the way for the development of high-power and high-energy rechargeable LABs.

4. Experimental Section

Materials: Lithium nitrate ($LiNO_3$, 99.0%, Kishida Chemical), lithium nitrite ($LiNO_2$, n-hydrate form, Mitsuwa Chemicals), and LiTFSI (99.95%, Kishida Chemical) were dehydrated overnight at 110 °C in a vacuum before being dissolved in solvents: DMF (super dehydrated grade, Fujifilm Wako Chemicals), DMA (super dehydrated grade, Fujifilm Wako Chemicals), DEA (>99.0%, Tokyo Chemical Industry), NMP (super dehydrated grade, Fujifilm Wako Chemicals), NEP (>98.0%, Tokyo Chemical Industry), NMPi (99%, Sigma-Aldrich), NMC (99%, Sigma-Aldrich), and TEG (lithium battery grade, Kishida Chemical) at a 1.0 M concentration. The resulting electrolytes were labeled as X–Y, where X indicates the solvent and Y refers to the salt anion. The H_2O content, measured using a Karl Fischer moisture meter (CA-31, Mitsubishi Chemical Corp.), was ≈150 ppm across all electrolytes. Single-walled CNTs (ZEONANO SG101, obtained from Sigma-Aldrich) were dispersed in deionized water at a concentration of 0.1 wt% using an ultrasonic homogenizer (450D, Branson). The slurry was then filtered through carbon paper (300 μm thick, Kureha Corp.) to obtain a CNT sheet cathode, which was supported on the carbon paper as a GDL. The CNT loading was 2.1 mg cm^{-2}, and the CNT layer thickness was ≈130 μm. The BET surface area was 910 $m^2 g^{-1}$ per the CNT loading weight, determined by the nitrogen adsorption isotherm at 77 K (3FLEX, Micromeritics).

Cell Assembly and Battery Testing: A stack-type LAB cell (the schematic illustration was shown in Figure S1, Supporting Information) was fabricated using a comprising layer of lithium foil (ϕ16 mm, 2.0 cm^2 electrode area, 200 μm thick, Honjo Metal), a porous polyolefin separator (20 μm thick, W-scope), and a CNT sheet cathode combined with a carbon paper GDL (ϕ16 mm) between two stainless steel plates. The separator and cathode were immersed in 32 μL of electrolyte, matching the void volume of the cathode and separator to prevent leakage. The total mass of the battery materials, including GDL carbon paper, CNT cathode, separator, Li foil, and electrolyte, was ≈70 mg. The assembled stack cell was sealed in a CR2032 coin cell configuration with a perforated mesh on the cathode side (50% aperture ratio, Hohsen Corp.). This design allows oxygen gas to flow through the gap between the hole mesh of the cathode case and the stainless steel plates sandwiching the stack cell components (Figure S1,

Supporting Information). The cell was placed in a 5 L air-tight chamber with a continuous pure oxygen flow of 150 mL min^{-1}. A homemade gravimetric analysis system, set at room temperature, was used to monitor the cell weight and voltage profile during battery operation.[26] The system involved a repeated weighing of the cell, connected to a battery-testing machine (ECAD-1000, EC Frontier), using a high-precision weight module (AD-4212B-23, A&D Co., Ltd.). Before discharging and charging, the cell was left in an OCV state for 48 h. The cell was then subjected to discharge–charge cycles at a constant current (0.8 mA × 5 h) within the voltage range of 2.0-4.5 V. The number of cell cycles was determined by the number of discharges that provided a 4 mAh (2 mAh cm^{-2} per electrode area) capacity, specifically, those discharges that reached the 2.0 V cutoff voltage minus one.

Characterization: The ionic conductivity, viscosity, and density of the electrolytes were measured using a pH/ion meter (SevenExcellence S500, Mettler Toledo) and a rolling ball viscometer (Lovis2000ME, Anton Paar), respectively. The HOMO–LUMO levels of the solvent molecules were calculated using the MOPAC software with the PM7 Hamiltonian. The conductor-like screening model (COSMO) was employed to reproduce solvent effects. LSV anodic scans were conducted with an electrochemical potentiostatic system (SP-50e, Biologic) at a scan rate of 0.1 mV s^{-1} from 2.95 V to 4.50 V. The cathode morphology and structures were analyzed using field-emission SEM (JSM-7800 F, JEOL, 5 keV accelerating voltage) equipped with an EDS analyzer (X-MaxN, Oxford Instruments). XRD measurement was carried out on an X-ray diffractometer (SmartLab, Rigaku) using a CuKα source (λCuKα = 1.542 Å).

Supporting Information

Supporting Information is available from the Wiley Online Library or from the author.

Acknowledgements

This study was partially supported by the JST Adaptable and Seamless Technology Transfer Program through Target-Driven Research and Development (A-STEP; grant no. JPMJTM22AQ), JSPS KAKENHI (grant nos. 24K08154 and 24K08585), and Japan Keirin Autorace (JKA) foundation (grant no. 2024M-380), and the National Institute for Materials Science (NIMS) Joint Research Hub Program. The authors thank Hisae Uematsu for the technical assistance. Material characterization and cell assembly were performed using the NIMS Battery Research Platform.

Conflict of Interest

The authors declare no conflict of interest.

Data Availability Statement

The data that support the findings of this study are available from the corresponding author upon reasonable request.

Keywords

amide-based electrolytes, carbon nanotubes, high-energy-density batteries, high-power batteries, lithium, lithium–air batteries, oxygen

Received: March 21, 2025
Revised: May 7, 2025
Published online:

[1] W. J. Kwak, Rosy, D. Sharon, C. Xia, H. Kim, L. R. Johnson, P. G. Bruce, L. F. Nazar, Y. K. Sun, A. A. Frimer, M. Noked, S. A. Freunberger, D. Aurbach, *Chem. Rev.* **2020**, *120*, 6626.
[2] J. O. Park, M. Kim, J. H. Kim, K. H. Choi, H. C. Lee, W. Choi, S. B. Ma, D. Im, *J. Power Sources* **2019**, *419*, 112.
[3] Y. Kubo, K. Ito, *ECS Transactions* **2014**, *62*, 129.
[4] S. Q. Zhao, L. Zhang, G. N. Zhang, H. B. Sun, J. Y. Yang, S. G. Lu, *J. Energy. Chem.* **2020**, *45*, 74.
[5] Z. Wen, Y. Liu, K. Li, S. Yang, H. Zhou, P. He, *National Science Review* **2025**, *12*, nwaf059.
[6] H. J. Kwon, H. C. Lee, J. Ko, I. S. Jung, H. C. Lee, H. Lee, M. Kim, D. J. Lee, H. Kim, T. Y. Kim, D. Im, *J. Power Sources* **2017**, *364*, 280.
[7] C. Z. Yang, R. A. Wong, M. S. Hong, K. Yamanaka, T. Ohta, H. R. Byon, *Nano Lett.* **2016**, *16*, 2969.
[8] X. Xin, K. Ito, Y. Kubo, *Electrochim. Acta* **2018**, *261*, 323.
[9] X. Gao, Y. Chen, L. Johnson, P. G. Bruce, *Nat. Mater.* **2016**, *15*, 918.
[10] S. B. Ma, D. J. Lee, V. Roev, D. Im, S. G. Doo, *J. Power Sources* **2013**, *244*, 494.
[11] K. Sakai, S. Iwamura, R. Sumida, I. Ogino, S. R. Mukai, *ACS Omega* **2018**, *3*, 691.
[12] A. Nomura, E. Mizuki, K. Ito, Y. Kubo, T. Yamagishi, M. Uejima, *Electrochim. Acta* **2021**, *400*, 139415.
[13] O. Wijaya, P. Hartmann, R. Younesi, I. I. E. Markovits, A. Rinaldi, J. Janek, R. Yazami, *J. Mater. Chem. A* **2015**, *3*, 19061.
[14] H. Wan, Q. Bai, Z. Peng, Y. Mao, Z. Liu, H. He, D. Wang, J. Xie, G. Wu, *J. Mater. Chem. A* **2017**, *5*, 24617.
[15] A. Nomura, S. Azuma, F. Ozawa, M. Saito, *J. Power Sources* **2025**, *633*, 236426.
[16] S. A. Freunberger, Y. H. Chen, N. E. Drewett, L. J. Hardwick, F. Barde, P. G. Bruce, *Angew. Chem. Int. Edit.* **2011**, *50*, 8609.
[17] C. Laoire, S. Mukerjee, E. J. Plichta, M. A. Hendrickson, K. M. Abraham, *J. Electrochem. Soc.* **2011**, *158*, A302.
[18] J. Uddin, V. S. Bryantsev, V. Giordani, W. Walker, G. V. Chase, D. Addison, *J. Phys. Chem. Lett.* **2013**, *4*, 3760.
[19] W. Walker, V. Giordani, J. Uddin, V. S. Bryantsev, G. V. Chase, D. Addison, *J. Am. Chem. Soc.* **2013**, *135*, 2076.
[20] D. W. Kim, D. H. Lee, S. M. Ahn, D. Y. Kim, J. Suk, D. H. Choi, Y. Kang, *J. Power Sources* **2017**, *347*, 186.
[21] C. Chen, L. Li, J. Su, C. Zhang, X. Chen, T. Huang, A. Yu, *Electrochim. Acta* **2017**, *243*, 357.
[22] S. Azuma, M. Sano, I. Moro, F. Ozawa, M. Saito, A. Nomura, *Electrochim. Acta* **2024**, *489*, 144261.
[23] V. S. Bryantsev, V. Giordani, W. Walker, M. Blanco, S. Zecevic, K. Sasaki, J. Uddin, D. Addison, G. V. Chase, *J. Phys. Chem. A* **2011**, *115*, 12399.
[24] H. Kwon, J. Baek, H.-T. Kim, *Energy Storage Materials* **2023**, *55*, 708.
[25] K. Nishioka, M. Tanaka, T. Goto, R. Haas, A. Henss, S. Azuma, M. Saito, S. Matsuda, W. Yu, H. Nishihara, H. Fujimoto, M. Tobisu, Y. Mukouyama, S. Nakanishi, *ACS Appl. Mater. Interfaces* **2024**, *16*, 46259.
[26] A. Nomura, K. Ito, D. Y. W. Yu, Y. Kubo, *J. Power Sources* **2024**, *592*, 233924.
[27] A. Smith, A. W. C. Menzies, *J. Am. Chem. Soc.* **1910**, *32*, 1412.
[28] F. J. Wilkins, *Nature* **1930**, *125*, 236.
[29] A. Wexler, *J. Res. Natl. Bur. Stand., A Phys. Chem.* **1976**, *80A*, 775.
[30] R. Viswanathan, T. S. L. Narasimhan, S. Nalini, *J. Phys. Chem. B* **2009**, *113*, 8362.
[31] F. Ozawa, K. Koyama, D. Iwasaki, S. Azuma, A. Nomura, M. Saito, *Electrochemistry* **2024**, *92*, 047003.
[32] M. Saito, T. Fujinami, M. Sohmiya, Y. Hayashi, H. Koyama, H. Otsuka, K. Ito, Y. Kubo, T. Horiba, *J. Electrochem. Soc.* **2021**, *168*, 010520.
[33] Y. Zhu, H. Sun, T. Zhang, Q. Li, Z. Xue, M. Yu, J. Li, X. Wang, *Langmuir* **2024**, *40*, 23511.

[34] Y. Pan, A. Hu, R. Xu, J. Chen, B. Yang, T. Li, K. Li, Y. Li, Z. W. Seh, J. Long, *ACS Sustain. Chem. Eng.* **2024**, *12*, 17177.
[35] X. Li, G. Zhang, D. Zhang, R. Yang, H. Yu, X. Zhang, G. Lian, H. Hou, Z. Guo, C. Hou, X. Yang, F. Dang, *Energy Environ. Sci.* **2024**, *17*, 8198.
[36] A. M. Stux, K. Swindler-Lyons, *Batteries*, Naval Research Laboratory, NRL/MR/6110—07-9073, **2007**, https://apps.dtic.mil/sti/citations/ADA472272.
[37] M. Tanaka, S. Inasawa, *Colloids Surf. A Physicochem. Eng. Asp.* **2023**, *672*, 131693.
[38] Y. Chen, S. A. Freunberger, Z. Peng, F. Bardé, P. G. Bruce, *J. Am. Chem. Soc.* **2012**, *134*, 7952.
[39] S. Freunberger, Y. Chen, N. E. Drewett, L. J. Hardwick, F. Bardé, P. G. Bruce. *Angew. Chem. Int. Ed.* **2011**, *50*, 8609.
[40] V. Bryanstev, V. Giordani, W. Walker, M. Blanco, S. Zecevic, K. Sasaki, J. Uddin, D. Addison, G. V. Chase, *J. Phys. Chem. A* **2011**, *115*, 12399.
[41] D. Sharon, D. Hirsberg, M. Afri, A. Garsuch, A. A. Frimer, D. Aurbach, *J. Phys. Chem. C* **2014**, *118*, 15207.
[42] J. Hassoun, F. Croce, M. Armand, B. Scrosati, *Angew. Chem. Int. Ed.* **2011**, *50*, 2999.
[43] M. Longo, M. Gandolfo, C. Francia, S. Bodoardo, M. Sangermano, J. Amici, *Electrochim. Acta* **2023**, *466*, 143026.
[44] Q. Chen, W. Tang, M. Kuai, G. Gao, Y. Hou, Q. Huang, W. Fang, Y. Chen, L. Liu, Y. Wu, *ACS Appl. Mater. Interfaces* **2025**, *17*, 16245.
[45] N. B. Aetukuri, B. D. McCloskey, J. M. Garcia, L. E. Krupp, V. Viswanathan, A. C. Luntz, *Nat. Chem.* **2015**, *7*, 50.
[46] K. P. C. Yao, D. G. Kwabi, R. A. Quinlan, A. N. Mansour, A. Grimaud, Y.-L. Lee, Y.-C. Lu, Y. Shao-Horn, *J. Electrochem. Soc.* **2013**, *160*, A824.
[47] B. Lee, J. Kim, G. Yoon, H.-D. Lim, I.-S. Choi, K. Kang, *Chem. Mat.* **2015**, *27*, 8406.
[48] S. T. Plunkett, H.-H. Wang, S. H. Park, Y. J. Lee, J. Cabana, K. Amine, S. Al-Hallaj, B. P. Chaplin, L. A. Curtiss, *ACS Appl. Energy Mater.* **2020**, *3*, 12575.
[49] R. R. Mitchell, B. M. Gallant, Y. Shao-Horn, C. V. Thompson, *J. Phys. Chem. Lett.* **2013**, *4*, 1060.
[50] S. Wu, J. Tang, F. Li, X. Liu, H. Zhou, *Chem. Commun.* **2015**, *51*, 16860.
[51] M. Saito, Y. Tachikawa, T. Fujinami, K. Mikami, Y. Hayashi, H. Shiroishi, D. Streich, E. J. Berg, P. Novak, *Electrochemistry* **2018**, *86*, 265.
[52] A. Dutta, K. Ito, A. Nomura, Y. Kubo, *Adv. Sci.* **2020**, *7*, 2001660.
[53] S. Azuma, M. Sano, I. Moro, F. Ozawa, M. Saito, A. Nomura, *J. Phys. Chem. C* **2023**, *127*, 7087.
[54] S. Azuma, I. Moro, M. Sano, F. Ozawa, M. Saito, A. Nomura, *J. Electrochem. Soc.* **2024**, *171*, 100511.
[55] J.-J. Xu, Z.-W. Chang, Y. Wang, D.-P. Liu, Y. Zhang, X.-B. Zhang, *Adv. Mater.* **2016**, *28*, 9620.